

UniSDF: Unifying Neural Representations for High-Fidelity 3D Reconstruction of Complex Scenes with Reflections

Fangjinhua Wang^{1,2*} Marie-Julie Rakotosaona² Michael Niemeyer² Richard Szeliski²
 Marc Pollefeys¹ Federico Tombari²
¹ETH Zürich ²Google

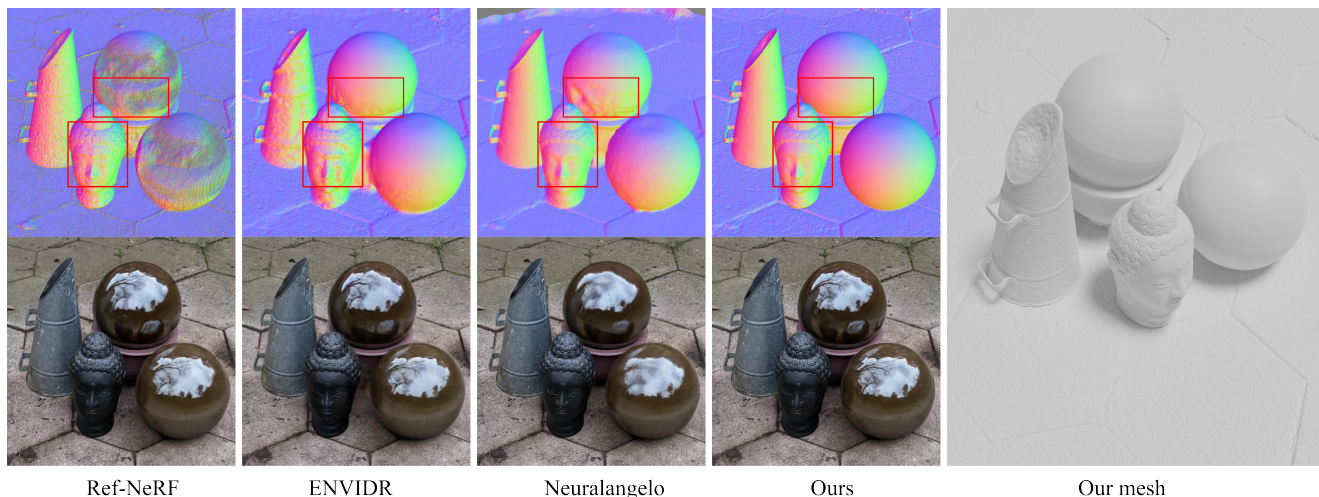


Figure 1. Comparison of surface normals (top) and RGB renderings (bottom) on “garden spheres” [37]. While the state-of-the-art methods Ref-NeRF [37], ENVIDR [18], and Neuralangelo [17] struggle to reconstruct reflective elements or fine geometric details, our method accurately models both, leading to high-quality mesh reconstructions of all parts of the scene. Best viewed when zoomed in.

Abstract

Neural 3D scene representations have shown great potential for 3D reconstruction from 2D images. However, reconstructing real-world captures of complex scenes still remains a challenge. Existing generic 3D reconstruction methods often struggle to represent fine geometric details and do not adequately model reflective surfaces of large-scale scenes. Techniques that explicitly focus on reflective surfaces can model complex and detailed reflections by exploiting better reflection parameterizations. However, we observe that these methods are often not robust in real unbounded scenarios where non-reflective as well as reflective components are present. In this work, we propose UniSDF, a general purpose 3D reconstruction method that can reconstruct large complex scenes with reflections. We investigate both view-based as well as reflection-based color prediction parameterization techniques and find that

explicitly blending these representations in 3D space enables reconstruction of surfaces that are more geometrically accurate, especially for reflective surfaces. We further combine this representation with a multi-resolution grid backbone that is trained in a coarse-to-fine manner, enabling faster reconstructions than prior methods. Extensive experiments on object-level datasets DTU, Shiny Blender as well as unbounded datasets Mip-NeRF 360 and Ref-NeRF real demonstrate that our method is able to robustly reconstruct complex large-scale scenes with fine details and reflective surfaces. Please see our project page at <https://fangjinhuaawang.github.io/UniSDF>.

1. Introduction

Given multiple images of a scene, accurately reconstructing a 3D scene is an open problem in 3D computer vision. 3D meshes from reconstruction methods can be used in many downstream applications, e.g. scene understanding,

*This work was conducted during an internship at Google.

robotics, and creating 3D experiences for augmented/virtual reality [31, 44]. Typical aspects of real-world scenes such as uniformly colored areas or non-Lambertian surfaces remain challenging.

As a traditional line of research, multi-view stereo methods [13, 33, 38, 42] usually estimate depth maps with photometric consistency and then reconstruct the surface as a post-processing step, *e.g.* point cloud fusion with screened Poisson surface reconstruction [15] or TSDF fusion [9]. However, they are unable to reconstruct reflective surfaces since their appearances are not multi-view consistent.

Recently, Neural Radiance Fields (NeRF) [22] render compelling photo-realistic images by parameterizing a scene as a continuous function of radiance and volume density using a multi-layer perceptron (MLP). More recent works [4, 7, 24, 35] replace or augment MLPs with grid based data structures to accelerate training. For example, Instant-NGP (iNGP) [24] uses a pyramid of grids and hashes to encode features and a tiny MLP to process them. Motivated by NeRF, neural implicit reconstruction methods [40, 43] combine signed distance functions (SDF) with volume rendering, and produce smooth and complete surfaces. For acceleration, recent works [17, 32] rely on hash grid representations and reconstruct surfaces with finer details. However, these NeRF-based methods cannot accurately reconstruct reflective surfaces.

To better capture the appearance of reflective surfaces, Ref-NeRF [37] computes the color with separate diffuse and specular components and parameterizes the appearance using reflected view that exploits the surface normals. BakedSDF [44] adopts the same Ref-NeRF components with a VolSDF [43] backbone to reconstruct large-scale scenes with shiny surfaces. However, BakedSDF is slow to train and struggles with reconstructing fine details.

We observe that while reflected view radiance fields can effectively reconstruct highly specular reflections, they struggle to represent more diffuse or ambiguous reflection types that can be found in real scenes. In contrast, we find that direct camera view radiance fields are more robust to difficult surfaces in real settings, although the reconstructions still present artifacts for reflective scenes. In this paper, we seamlessly bring together geometry based reflected view radiance fields and camera view-based radiance fields into a novel unified radiance field for representing 3D real scenes accurately in the presence of reflections. Our method is robust for reconstructing both real challenging scenes and highly reflective surfaces.

The proposed method, named UniSDF, achieves state-of-the-art performance on DTU [1], Shiny Blender [37], Mip-NeRF 360 dataset [3] and Ref-NeRF real dataset [37]. It demonstrates the capability to accurately reconstruct complex scenes with large scale, fine details and reflective surfaces as we see in Fig. 1. Our contributions are summa-

rized as follows:

- We propose a novel algorithm that learns to seamlessly combine two radiance fields in 3D while exploiting the advantages of each representation. Our method produces high quality object surfaces in both reflective and non-reflective regions.
- Ours method relies on a hash grid backbone that enables fast training while maintaining high reconstruction quality. Moreover, our pipeline is robust and does not require large amounts of parameter tuning.

2. Related Works

Multi-view stereo (MVS). Many traditional [33, 41] and learning-based [13, 38, 39, 42] MVS methods first estimate multi-view depth maps and then reconstruct the surface by fusing depth maps in a post-processing step. As the core step, depth estimation is mainly based on the photometric consistency assumption across multiple views. However, this assumption fails for glossy surfaces with reflections, and thus MVS methods cannot reconstruct them accurately.

Neural radiance fields (NeRF). As a seminal method in view synthesis, NeRF [22] represents a scene as a continuous volumetric field with an MLP, with position and camera view direction as inputs, and renders an image using volumetric ray-tracing. Since NeRF is slow to train, some methods [7, 24, 35] use voxel-grid-like data structures to accelerate training. Many follow-up works apply NeRFs to different tasks, *e.g.* sparse-view synthesis [26, 36, 46], real-time rendering [8, 14, 29, 45], 3D generation [6, 20, 28] and pose estimation [19, 34, 49]. For the 3D reconstruction task, there are many methods [11, 17, 21, 27, 30, 32, 40, 43, 47] integrating NeRF with signed distance functions, a common implicit function for geometry. Specifically, they transform SDFs back to volume density for volume rendering. However, we observe that they are unable to reconstruct shiny / reflective surfaces since NeRF’s camera view direction parameterization for the color prediction does not accurately model reflective parts of the scene.

NeRFs for reflections. Recently, Ref-NeRF [37] reparameterizes the appearance prediction with separate diffuse and reflective components by using the reflected view direction, which improves the rendering of specular surfaces. As a result, recent works such as BakedSDF [44] or ENVIDR [18] adopt this representation to reconstruct glossy surfaces of unbounded scenes and with material decomposition, respectively. While leading to strong view-synthesis results for reflective areas, we find that reflective radiance field approaches often lead to overly smooth reconstructions with missing details and that their optimization is not stable on real-world scenes. In contrast to existing methods with a

single radiance field, we propose to seamlessly combine reflected view radiance fields and camera view based radiance fields into a novel unified radiance field, which is robust for reconstruction in challenging scenes with highly reflective surfaces.

3. Method

In this section, we first review the basic elements of NeRF. We then describe the architecture and training strategy of our method.

3.1. NeRF Preliminaries

In NeRF [22], a 3D scene is represented by mapping a position \mathbf{x} and ray direction \mathbf{d} to a volumetric density σ and color \mathbf{c} using MLP. For a pixel in the target viewpoint and its corresponding ray $\mathbf{r} = \mathbf{o} + t\mathbf{d}$, distance values t_i are sampled along the ray. The density σ_i is predicted by a spatial MLP that receives the position \mathbf{x} as input, while the directional MLP that predicts the color \mathbf{c}_i uses the bottleneck vector $\mathbf{b}(\mathbf{x})$ from the density MLP and the view direction \mathbf{d} as input. The final color \mathbf{C} is rendered as:

$$\mathbf{C} = \sum_i w_i \mathbf{c}_i, w_i = T_i \alpha_i, \quad (1)$$

where $\alpha_i = 1 - \exp(-\sigma_i \delta_i)$ is opacity, $\delta_i = t_i - t_{i-1}$ is the distance between adjacent samples, and $T_i = \prod_{j=1}^{i-1} (1 - \alpha_j)$ is the accumulated transmittance. The model is trained by minimizing the loss between the predicted and ground truth color:

$$\mathcal{L}_{\text{color}} = \mathbb{E}[\|\mathbf{C} - \mathbf{C}_{gt}\|^2]. \quad (2)$$

Note that Mildenhall *et al.* [22] uses a single-layer directional MLP and thus often describes the combination of NeRF’s spatial and view dependence MLPs as a single MLP.

3.2. UniSDF

Given a set of known images of a scene that potentially contains reflective surfaces, our goal is to optimize a neural implicit field and reconstruct the scene with high fidelity and geometric accuracy. We propose UniSDF, a method that enables us to seamlessly combine camera view radiance fields and reflected view radiance fields to reconstruct both (a) non-reflective surfaces, diffuse reflective surfaces and complex surfaces with both reflective and non-reflective areas as well as (b) highly specular surfaces with a well defined and detailed reflected environment. Our pipeline is shown in Fig. 2. We generate two radiance fields that are parameterized by camera view directions or reflected directions and combine them at the pixel level using a learned rendered weight.

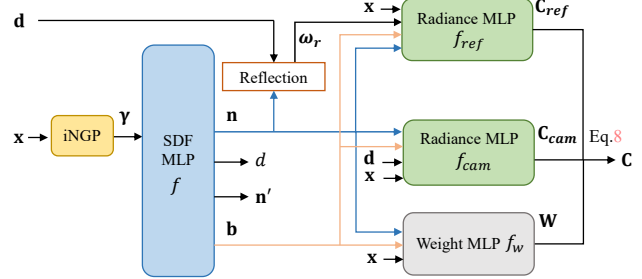


Figure 2. Pipeline of UniSDF. We combine the camera radiance field and the reflected radiance field in 3D. Given a position \mathbf{x} , we extract iNGP features γ and input them to an MLP f that estimates a signed distance value d used to compute the NeRF density. We parametrize the camera view and reflected view radiance fields with two different MLPs f_{cam} and f_{ref} respectively. Finally, we learn a continuous weight field that is used to compute the final color as a weighted composite \mathbf{W} of the radiance fields colors \mathbf{C}_{cam} and \mathbf{C}_{ref} after volume rendering, Eq. 8.

Volume rendering the SDF. We represent the scene geometry using a signed distance field (SDF), which defines the surface \mathcal{S} as the zero level set of the SDF d :

$$\mathcal{S} = \{\mathbf{x} : d(\mathbf{x}) = 0\} \quad (3)$$

To better reconstruct large-scale scenes, we follow Mip-NeRF 360 [3] and transform \mathbf{x} into a *contracted space* with the following contraction:

$$\text{contract}(\mathbf{x}) = \begin{cases} \mathbf{x} & \|\mathbf{x}\| \leq 1 \\ \left(2 - \frac{1}{\|\mathbf{x}\|}\right) \left(\frac{\mathbf{x}}{\|\mathbf{x}\|}\right) & \|\mathbf{x}\| > 1 \end{cases} \quad (4)$$

For volume rendering, we compute the volume density $\sigma(\mathbf{x})$ from the signed distance $d(\mathbf{x})$ as: $\sigma(\mathbf{x}) = \alpha \Psi_\beta(d(\mathbf{x}))$, where Ψ_β is the cumulative distribution function of a zero-mean Laplace distribution with learnable scale parameter $\beta > 0$. The surface normal at \mathbf{x} can be computed as the gradient of the signed distance field: $\mathbf{n} = \nabla d(\mathbf{x}) / \|\nabla d(\mathbf{x})\|$.

Hash Encoding with iNGP. To accelerate training and improve reconstruction of high-frequency details, we use iNGP [24] to map each position \mathbf{x} to a higher-dimensional feature space. Specifically, the features $\{\gamma_l(\mathbf{x})\}$ from the pyramid levels of iNGP are extracted with trilinear interpolation and then concatenated to form one single feature vector $\gamma(\mathbf{x})$, which is passed to the SDF MLP.

Camera View & Reflected View Radiance Fields. In contrast to most existing NeRF methods [2, 22, 37] that use a single radiance field, we propose to combine a camera view radiance field and a reflected view radiance field to better represent reflective and non reflective surfaces.

We follow NeRF [22] for representing our camera view radiance field \mathbf{c}_{cam} , which is computed from features defined at each position and the camera view direction:

$$\mathbf{c}_{cam} = f_{cam}(\mathbf{x}, \mathbf{d}, \mathbf{n}, \mathbf{b}), \quad (5)$$

where \mathbf{b} is the bottleneck feature vector from SDF MLP, \mathbf{n} is the normal at \mathbf{x} and \mathbf{d} is the view direction. Similarly to recent works [40, 43], we notice that using surface normals as input leads to better quality.

We represent the reflected radiance field \mathbf{c}_{ref} with an MLP f_{ref} as:

$$\mathbf{c}_{ref} = f_{ref}(\mathbf{x}, \omega_r, \mathbf{n}, \mathbf{b}), \quad (6)$$

where ω_r is the reflected view direction around the normal \mathbf{n} . Unlike Ref-NeRF [37], which uses separate diffuse and specular components, we only use the specular component, leading to a simpler architecture. Additionally, we observe that using separate diffuse and specular components can lead to optimization instabilities resulting in geometry artifacts (see also Fig. 11).

The main difference between the two radiance fields is the view directional input of the MLP. We visualize the rendered color for two radiance fields and surface normal in Fig. 3. Observe that our method mainly uses the reflected radiance field to represent highly specular reflections such as the tree reflections in the garden spheres or the environment reflection on the sedan car. The camera view radiance field is used to represent more diffuse reflections. Fig. 4 illustrates these observations, where we show the weight for reflected view radiance field. We can observe that more reflective parts of the scene tend to be represented with reflected radiance (red). Moreover, the normal maps of our method show that our model accurately reconstructs reflective and non-reflective surface geometry.

Learned composition. We compose the two radiance fields using a learned weight field in 3D. We use an MLP f_w to learn the weight values \mathbf{w} :

$$\mathbf{w} = \text{sigmoid}(f_w(\mathbf{x}, \mathbf{n}, \mathbf{b})). \quad (7)$$

We compose the signals at the pixel level. We first volume render \mathbf{W} , \mathbf{C}_{ref} , \mathbf{C}_{cam} following Eq. 1. We then compose the colors for each pixel as follows:

$$\mathbf{C} = \mathbf{W} \cdot \mathbf{C}_{ref} + (1 - \mathbf{W}) \cdot \mathbf{C}_{cam}. \quad (8)$$

Motivation of dual radiance fields. Disambiguating the influence of geometry, color and reflections is an ill posed problem in 3D reconstruction from 2D images. We observe in Fig. 8 that when using a single camera view radiance field (CamV) or a single reflected view radiance field with a diffuse and specular decomposition similar to Ref-NeRF [37]

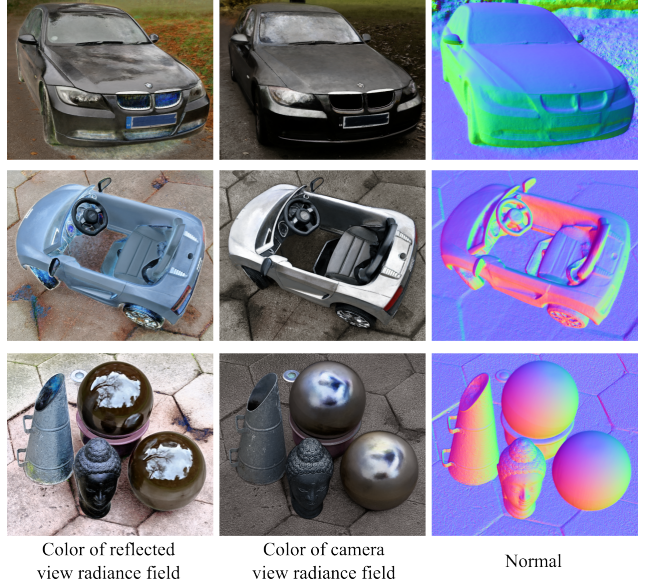


Figure 3. Visualization of our color of reflected view radiance field, color of camera view radiance field and normal on “sedan”, “toycar” and “garden spheres” scenes [37].

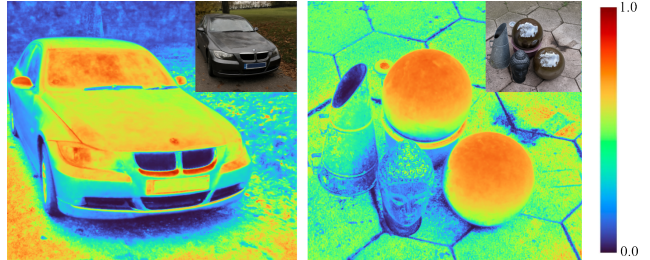


Figure 4. Visualization of our learned weight \mathbf{W} for reflected view radiance field on “sedan” and “garden spheres” scenes [37]. Our method assigns high weight for reflective surfaces, *e.g.* window and hood of car, spheres.

(RefV) with our backbone, appearance effects such as view dependencies or reflections are sometimes wrongly represented by inaccurate geometry. These limitations are also common in recent methods such as BakedSDF [44], as we can see in Fig. 7.

Moreover, since each type of radiance field is specialized for different levels of reflection strength and complexity, we observe that the reconstructed geometries while using the two types of radiance are often complementary (Fig. 8). In our method, we explicitly intertwine the radiance fields in 3D to continuously determine and use the most adapted parametrization for each surface area.

3.3. Training and Regularization

Coarse-to-fine training. We observe that directly optimizing all the features in our multi-resolution hash grid

leads to overfitting, in particular to specular appearance details, which in turn results in incorrect geometry as we show in Fig. 10. We observe that this model tends to fake specular effects by embedding emitters inside the surface exploiting the numerous learnable features in the hash grid.

Therefore, we propose to instead optimize the hash grid features in a coarse-to-fine fashion, similarly to [17, 32], to avoid overfitting and promote smoother and more realistic surfaces. Specifically, we start with L_{init} coarse pyramid levels in the beginning of training, and introduce a new level with higher resolution every T_0 training fraction (see implementation details).

Regularization. Following prior works [40, 43], we use an eikonal loss [12] to encourage $d(\mathbf{x})$ to approximate a valid SDF:

$$\mathcal{L}_{\text{eik}} = \mathbb{E}_{\mathbf{x}}[(\|\nabla d(\mathbf{x})\| - 1)^2]. \quad (9)$$

To promote normal smoothness, we constrain the computed surface normal \mathbf{n} to be close to a predicted normal vector \mathbf{n}' . \mathbf{n}' is predicted by the SDF MLP and normalized. We use the normal smoothness loss \mathcal{L}_p [37] as:

$$\mathcal{L}_p = \sum_i w_i \|\mathbf{n} - \mathbf{n}'\|^2. \quad (10)$$

We also use the orientation loss \mathcal{L}_o from Ref-NeRF [37] to penalize normals that are “back-facing”, using:

$$\mathcal{L}_o = \sum_i w_i \max(0, \mathbf{n} \cdot \mathbf{d})^2. \quad (11)$$

Full loss function. The full loss function \mathcal{L} includes the color loss $\mathcal{L}_{\text{color}}$ of composed color \mathbf{C} and the regularizations, which is written as follows:

$$\mathcal{L} = \mathcal{L}_{\text{color}} + \lambda_1 \mathcal{L}_{\text{eik}} + \lambda_2 \mathcal{L}_p + \lambda_3 \mathcal{L}_o. \quad (12)$$

4. Experiments

4.1. Experimental Settings

Datasets. We evaluate our method on four different types of datasets. The DTU dataset [1] is an indoor object-centric multi-view stereo dataset with ground truth point clouds. Following prior works [40, 43], we use the same 15 scenes for evaluation. The Shiny Blender dataset is proposed in [37] and contains six different shiny objects that are rendered in Blender under conditions similar to the NeRF dataset. The Mip-NeRF 360 dataset is proposed in [3] and contains complex unbounded indoor and outdoor scenes captured from many viewing angles. We further evaluate on the three real world scenes with reflections that are introduced in Ref-NeRF [37], which consists of the scenes “sedan”, “garden shperes” and “toy car”. For simplicity, we name these 3 scenes the “Ref-NeRF real dataset”.

Implementation details. Based on the Mip-NeRF 360 codebase [23], we implement our method in Jax [5] with the re-implementation of VolSDF [43] and iNGP [24]. In our iNGP hierarchy of grids and hashes, we use 15 levels from 32 to 4096, where each level has 4 channels. For coarse to fine training, we set $L_{\text{init}} = 4$ and $T_0 = 2\%$. Similar to mip-NeRF 360 [3], we use two rounds of proposal sampling and then a final NeRF sampling round. Following Zip-NeRF, we penalize the sum of the mean of squared grid/hash values at each pyramid level with a loss multiplier as 0.1. Our models are all trained on 8 NVIDIA Tesla V100-SXM2-16GB GPUs with a batch size of 2^{14} . We train 25k steps on DTU / Shiny Blender and 100k steps on 360 / Ref-NeRF real datasets, which takes 0.75h and 3.50h respectively. See the supplement for more details.

Baselines. We compare our method to state-of-the-art methods in view synthesis [3, 4, 24, 37] and implicit reconstruction [17, 18, 32, 44]. Zip-NeRF [4] and Neuralangelo [17] are hash grid-based top performing methods for view synthesis and reconstruction, respectively. BakedSDF [44] integrates VolSDF, Ref-NeRF and Mip-NeRF 360 to reconstruct high quality mesh for unbounded scenes with reflective surfaces. ENVIDR [18] is a top performing method for reconstructing and rendering specular surfaces that integrates VolSDF, Ref-NeRF, iNGP and an environment MLP for lighting. Note that this method relies on explicitly supervising the renderer training with ground truth materials, which we do not rely on.

We train Neuralangelo with batch size as 2^{11} for 800k iterations on the Ref-NeRF real dataset, which takes about 58 hours on an NVIDIA 3090 GPU for each scene. We also train BakedSDF [44] on the Shiny Blender and Ref-NeRF real datasets with a batch size of 2^{14} for 250k iterations. As we find that BakedSDF’s optimization is unstable on these complex scenes and results degrade with default parameters, we carefully tune its hyperparameters for each scene and report best results (see sup. mat. for details).

To further evaluate the effectiveness of our method, we propose two custom baselines, named “CamV” and “RefV”. Using the same backbone as our method, “CamV” uses only the camera view radiance field, while “RefV” uses only the reflected view radiance field following Ref-NeRF [37]. Note that for both baselines, we also use our coarse-to-fine training strategy to improve performance.

4.2. Evaluation Results

DTU. We evaluate the accuracy of 3D reconstruction on the DTU dataset [1]. Similar to NeuS [40], we use an additional NeRF network to model the background with the coordinate contraction from Mip-NeRF 360 [3]. Following prior works, we extract the mesh at 512 resolution. We summarize the quantitative results in Table 1. For Neuralan-

Methods	Chamfer Distance (mm) ↓
VolSDF [43]	0.86
NeuS [40]	0.87
NeuralWarp [10]	0.68
Neuralangelo [17]	1.07
PermutoSDF [32]	0.68
Ours	0.64

Table 1. Quantitative reconstruction results on DTU dataset [1]. Best score is in bold.

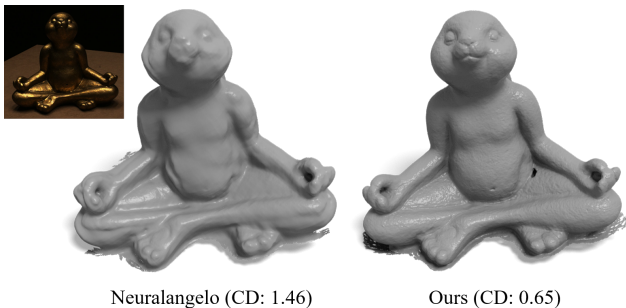


Figure 5. Visualization and Chamfer Distance error (CD) of reconstructions on DTU scan 110. Our method produces smooth surface with more details, while Neuralangelo [17] outputs an over-smoothed surface. Best viewed when zoomed in.

Methods	PSNR ↑	SSIM ↑	LPIPS ↓	MAE ^o ↓
NVDiffRec [25]	28.70	0.945	0.119	17.05
Ref-NeRF [37]	35.96	0.967	0.058	18.38
ENVIDR [18]	35.85	0.983	0.036	4.61
Ours	36.82	0.976	0.043	4.76

Table 2. Quantitative results on Shiny Blender [37]. Red, orange, and yellow indicate the first, second, and third best performing algorithms for each metric.

gelo [17], we report the reproduced results from their official implementation. Our method achieves state-of-the-art performance when compared with other methods. We visualize the qualitative results on DTU scan 110 in Fig. 5. Our method reconstructs the surface with more details and fewer artifacts than Neuralangelo [17].

Shiny Blender. We summarize the rendering metrics (PSNR, SSIM, LPIPS) and mean angular error (MAE) in Table 2. Note that although running intensive hyperparameter searches, we could not find stable settings for BakedSDF [44] on the “car” and “teapot” scenes (please see supp. mat. for details). Our method performs best in PSNR and performs on par with ENVIDR [18] in SSIM, LPIPS and MAE. Note that ENVIDR additionally uses an environment MLP and relies on extra supervision with ground truth materials, which we do not require, to improve rendering and reconstruction. As shown in Fig. 6, BakedSDF [44] reconstructs an erroneous hole in the front and incorrect sur-

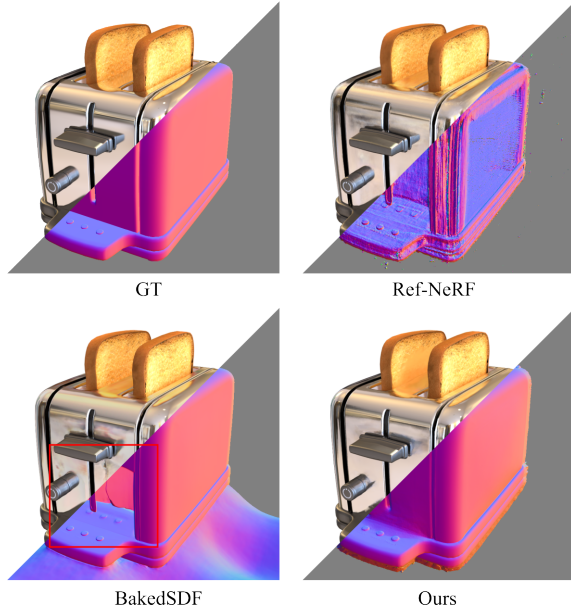


Figure 6. Qualitative comparison on “toaster” scene [37]. Our method reconstructs more accurate surface for the shiny object, while BakedSDF [44] fakes specular effects by embedding emitters inside the reflective surface (highlighted with red box) and reconstructs extra geometry below the object.

face elements under the object, while our method reconstructs the reflective surface more accurately.

Mip-NeRF 360 dataset. As shown in Table 3, our method ranks second on outdoor scenes and third on indoor scenes. Note that state-of-the-art Zip-NeRF [4] focuses on image rendering while we focus on high-quality geometric reconstruction. Compared with BakedSDF [44], our performance is significantly better in all metrics. As shown in Fig. 7, our method reconstructs more complete surfaces and better details, while BakedSDF shows hole artifacts in some regions and struggles to reconstruct fine geometric details.

Ref-NeRF real dataset. We summarize the rendering metrics in Table 4. Our method outperforms Ref-NeRF [37] and Neuralangelo [17] in both SSIM and LPIPS, and BakedSDF [44] in LPIPS. As shown in Fig. 1, though ENVIDR [18] performs well on Shiny Blender [37], it has similar artifacts on the spheres as Neuralangelo [17]. Our method accurately reconstructs the smooth surface of the reflective spheres and the fine details on the statue. We visualize the weight \mathbf{W} for our reflected radiance \mathbf{C}_{ref} in Fig. 4. Our method automatically assigns high weights for the reflective view radiance field on the shiny surfaces, which encourages it to model reflections, as shown in Fig. 3.

Methods	Outdoor Scenes			Indoor Scenes		
	PSNR \uparrow	SSIM \uparrow	LPIPS \downarrow	PSNR \uparrow	SSIM \uparrow	LPIPS \downarrow
NeRF [22]	21.46	0.458	0.515	26.84	0.790	0.370
NeRF++ [48]	22.76	0.548	0.427	28.05	0.836	0.309
Mip-NeRF 360 [3]	24.47	0.691	0.283	31.72	0.917	0.180
Instant-NGP [24]	22.90	0.566	0.371	29.15	0.880	0.216
MERF [29]	23.19	0.616	0.343	27.80	0.855	0.271
Zip-NeRF [4]	25.56	0.750	0.207	32.25	0.926	0.168
BakedSDF [44]	23.40	0.619	0.379	30.21	0.888	0.243
Ours	24.77	0.723	0.241	31.28	0.915	0.180

Table 3. Quantitative results on the “outdoor” and “indoor” scenes of Mip-NeRF 360 dataset [3]. Red, orange, and yellow indicate the first, second, and third best performing algorithms for each metric.

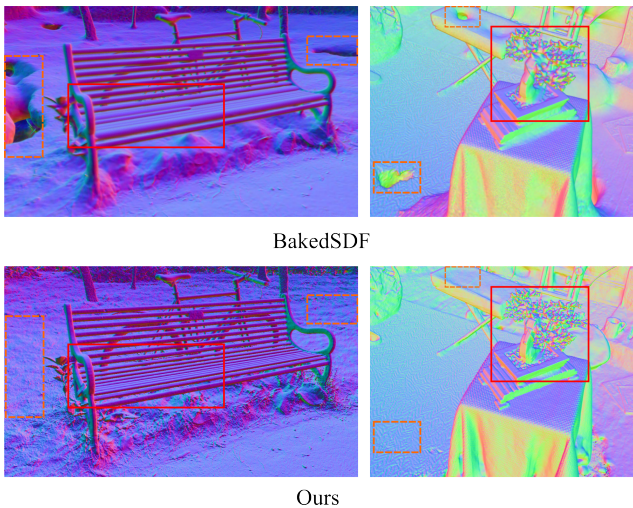


Figure 7. Qualitative comparison with BakedSDF [44] on “bicycle” and “officebonsai” scene of Mip-NeRF 360 dataset [3]. BakedSDF produces hole structures in many regions (highlighted with dotted orange boxes) and less details of fine structures (highlighted with red boxes), while our method reconstructs more complete surfaces and better details. Best viewed when zoomed in.

Methods	PSNR \uparrow	SSIM \uparrow	LPIPS \downarrow
Mip-NeRF 360 [3]	24.27	0.650	0.276
Ref-NeRF [37]	24.06	0.589	0.355
Zip-NeRF [4]	23.68	0.635	0.247
Neuralangelo [17]	23.70	0.608	0.330
BakedSDF [44]	24.43	0.636	0.325
Ours	23.70	0.636	0.265

Table 4. Quantitative results on the Ref-NeRF real dataset [37]. Red, orange, and yellow indicate the first, second, and third best performing algorithms for each metric.

Custom baselines comparison. We compare our method with our two custom baselines on the DTU [1], Mip-NeRF 360 [3], and Ref-NeRF real [37] datasets. As shown in Table 5, our method outperforms the two baselines in all metrics on all three datasets. CamV mostly outperforms RefV, while RefV fails on one scene in DTU. This shows that the camera view radiance field is usually more robust than the

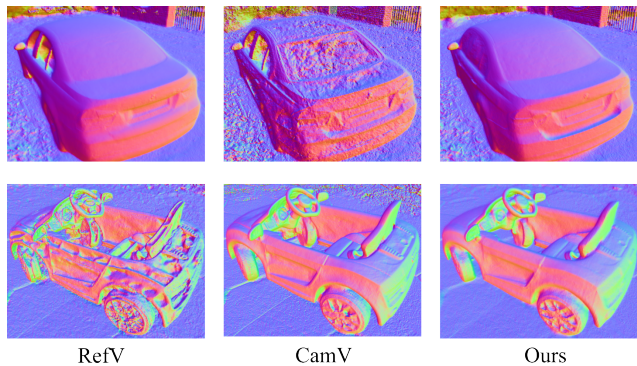


Figure 8. Qualitative comparison with two baselines, RefV and CamV on “sedan” and “toycar” scene [37]. . Best viewed when zoomed in.

reflected view radiance field, although this method does not reconstruct the geometry of reflective regions well.

Fig. 8 shows a qualitative comparison, where RefV reconstructs smooth surface for the reflective back window but has artifacts on the side for “sedan”, while CamV fails to reconstruct accurate surfaces because of the reflections. On the “toycar” scene, RefV fails to reconstruct the correct geometry, while CamV reconstructs shiny surfaces better while showing artifacts on the hood. For RefV, we sometimes observe optimization issues with separate diffuse and specular components, where the specular component may be blank throughout training and the diffuse component (w/o. directional input) wrongly represents the view-dependent appearance with incorrect geometry (see sup. mat. for details). By coupling two difference radiance fields continuously in 3D, our method represents the appearance and geometry better than the baselines that only use a single radiance field, leading to higher-quality reconstructed surfaces.

Mesh visualization. We visualize our reconstructed meshes of unbounded outdoor and indoor scenes from [3] in Fig. 9. Our method is able to accurately reconstruct the scenes, including fine geometric details.

Methods	DTU	360 Outdoor Scenes			360 Indoor Scenes			Ref-NeRF real dataset		
	CD (mm) ↓	PSNR ↑	SSIM ↑	LPIPS ↓	PSNR ↑	SSIM ↑	LPIPS ↓	PSNR ↑	SSIM ↑	LPIPS ↓
CamV	0.85	24.42	0.712	0.257	30.81	0.909	0.184	23.30	0.622	0.283
RefV	0.89*	24.01	0.709	0.249	30.15	0.901	0.190	23.02	0.615	0.301
Ours	0.64	24.77	0.723	0.241	31.28	0.915	0.180	23.70	0.636	0.265

Table 5. Quantitative comparison with two custom baselines, CamV and RefV, on DTU [1], Mip-NeRF 360 dataset [3] and Ref-NeRF real dataset [37]. *: RefV fails on scan 110 of DTU, the reported chamfer distance (CD) is the average of other 14 scans. Best scores are in bold.

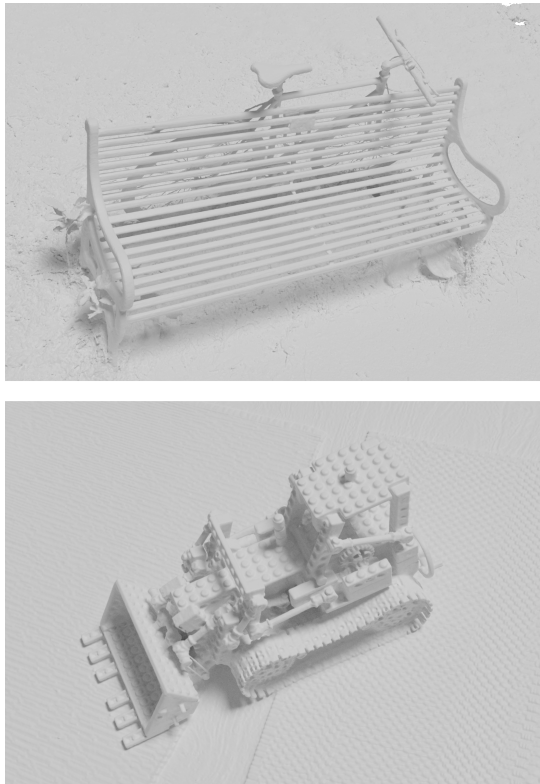


Figure 9. Visualization of our reconstructed mesh on “bicycle” and “kitchenlego” scene from [3]. Best viewed when zoomed in.

4.3. Ablation Study

Coarse-to-fine training. As shown in Fig. 10, the reconstructions contain artifacts on the specular window and hood without training in a coarse-to-fine manner. With all feature pyramid grids activated in the beginning, the hash grid backbone can easily overfit to the specular effects with wrong geometry.

Diffuse component in Reflected View Radiance Field.

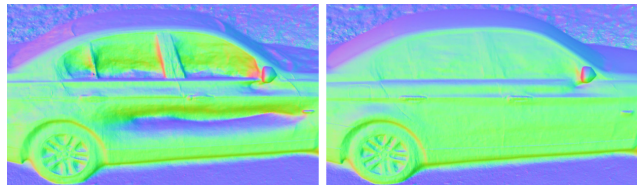
Recall that we only use the specular component with reflected view direction as input. We find that adding an additional diffuse component that depends on the position only as proposed in [37] leads to artifacts in the reconstructions (see e.g. the side of the car in Fig. 11), while our method produces a more complete and accurate surface.



w/o. coarse-to-fine training

ours

Figure 10. Ablation of coarse-to-fine training on “sedan” scene [37]. Without coarse-to-fine training, the model overfits to the specular appearance of the car with incorrect geometry, while our method reconstruct the shiny surface more accurately.



w. diffuse component

ours

Figure 11. Ablation of diffuse component in reflected view radiance field on “sedan” scene [37]. An additional diffuse component in the reflected view radiance field as in [37] leads to artifacts on the surface of car, while our method outputs more accurate surfaces.

5. Conclusion

In this paper, we have presented UniSDF, a novel algorithm that learns to seamlessly combine radiance fields for robust and accurate reconstruction of complex scenes with reflections. We find that camera view radiance fields, e.g. NeRF, are robust to complex real settings but cannot reconstruct reflective surfaces well, while reflective radiance fields, e.g. Ref-NeRF, can effectively reconstruct highly specular surfaces but struggle in real-world settings and to represent other types of surfaces. By adaptively combining camera view radiance fields and reflective radiance fields in 3D, our method significantly outperforms the baselines with either single radiance field. Together with a hash grid backbone to accelerate training and improve reconstruction details, our method achieves state-of-the-art performance in reconstruction and rendering on object-level and unbounded scenes.

Acknowledgement. We would like to thank Dor Verbin, Peter Hedman, Ben Mildenhall and Pratul P. Srinivasan for feedback and comments.

References

- [1] Henrik Aanæs, Rasmus Ramsbøl Jensen, George Vogiatzis, Engin Tola, and Anders Bjorholm Dahl. Large-scale data for multiple-view stereopsis. *IJCV*, 2016. 2, 5, 6, 7, 8, 1, 3
- [2] Jonathan T Barron, Ben Mildenhall, Matthew Tancik, Peter Hedman, Ricardo Martin-Brualla, and Pratul P Srinivasan. Mip-NeRF: A multiscale representation for anti-aliasing neural radiance fields. In *Proceedings of the IEEE/CVF International Conference on Computer Vision*, pages 5855–5864, 2021. 3
- [3] Jonathan T Barron, Ben Mildenhall, Dor Verbin, Pratul P Srinivasan, and Peter Hedman. Mip-NeRF 360: Unbounded anti-aliased neural radiance fields. In *Proceedings of the IEEE/CVF Conference on Computer Vision and Pattern Recognition*, pages 5470–5479, 2022. 2, 3, 5, 7, 8, 1
- [4] Jonathan T Barron, Ben Mildenhall, Dor Verbin, Pratul P Srinivasan, and Peter Hedman. Zip-NeRF: Anti-aliased grid-based neural radiance fields. *arXiv preprint arXiv:2304.06706*, 2023. 2, 5, 6, 7, 1
- [5] James Bradbury, Roy Frostig, Peter Hawkins, Matthew J. Johnson, Chris Leary, Dougal Maclaurin, George Necula, Adam Paszke, Jake VanderPlas, Skye Wanderman-Milne, and Qiao Zhang. JAX: composable transformations of Python+NumPy programs, 2018. 5
- [6] Eric R Chan, Connor Z Lin, Matthew A Chan, Koki Nagano, Boxiao Pan, Shalini De Mello, Orazio Gallo, Leonidas J Guibas, Jonathan Tremblay, Sameh Khamis, et al. Efficient geometry-aware 3d generative adversarial networks. In *Proceedings of the IEEE/CVF Conference on Computer Vision and Pattern Recognition*, pages 16123–16133, 2022. 2
- [7] Anpei Chen, Zexiang Xu, Andreas Geiger, Jingyi Yu, and Hao Su. TensorRF: Tensorial radiance fields. In *European Conference on Computer Vision*, pages 333–350. Springer, 2022. 2
- [8] Zhiqin Chen, Thomas Funkhouser, Peter Hedman, and Andrea Tagliasacchi. MobileNeRF: Exploiting the polygon rasterization pipeline for efficient neural field rendering on mobile architectures. In *Proceedings of the IEEE/CVF Conference on Computer Vision and Pattern Recognition*, pages 16569–16578, 2023. 2
- [9] Brian Curless and Marc Levoy. A volumetric method for building complex models from range images. In *Proceedings of the 23rd annual conference on Computer graphics and interactive techniques*, pages 303–312, 1996. 2
- [10] François Darmon, Bénédicte Bascle, Jean-Clément Devaux, Pascal Monasse, and Mathieu Aubry. Improving neural implicit surfaces geometry with patch warping. In *Proceedings of the IEEE/CVF Conference on Computer Vision and Pattern Recognition*, pages 6260–6269, 2022. 6, 3
- [11] Qiancheng Fu, Qingshan Xu, Yew Soon Ong, and Wenbing Tao. Geo-Neus: Geometry-consistent neural implicit surfaces learning for multi-view reconstruction. *Advances in Neural Information Processing Systems*, 35:3403–3416, 2022. 2
- [12] Amos Gropp, Lior Yariv, Niv Haim, Matan Atzmon, and Yaron Lipman. Implicit geometric regularization for learning shapes. *arXiv preprint arXiv:2002.10099*, 2020. 5
- [13] Xiaodong Gu, Zhiwen Fan, Siyu Zhu, Zuo Zhuo Dai, Feitong Tan, and Ping Tan. Cascade cost volume for high-resolution multi-view stereo and stereo matching. In *Proceedings of the IEEE/CVF conference on computer vision and pattern recognition*, pages 2495–2504, 2020. 2
- [14] Peter Hedman, Pratul P Srinivasan, Ben Mildenhall, Jonathan T Barron, and Paul Debevec. Baking neural radiance fields for real-time view synthesis. In *Proceedings of the IEEE/CVF International Conference on Computer Vision*, pages 5875–5884, 2021. 2
- [15] Michael Kazhdan and Hugues Hoppe. Screened Poisson surface reconstruction. *ACM Transactions on Graphics (ToG)*, 32(3):1–13, 2013. 2
- [16] Diederik P. Kingma and Jimmy Ba. Adam: A method for stochastic optimization. *ICLR*, 2015. 1
- [17] Zhaoshuo Li, Thomas Müller, Alex Evans, Russell H Taylor, Mathias Unberath, Ming-Yu Liu, and Chen-Hsuan Lin. Neuralangelo: High-fidelity neural surface reconstruction. In *Proceedings of the IEEE/CVF Conference on Computer Vision and Pattern Recognition*, pages 8456–8465, 2023. 1, 2, 5, 6, 7, 3
- [18] Ruofan Liang, Huiting Chen, Chunlin Li, Fan Chen, Selvakumar Panneer, and Nandita Vijaykumar. ENVIDR: Implicit differentiable renderer with neural environment lighting. *arXiv preprint arXiv:2303.13022*, 2023. 1, 2, 5, 6, 4
- [19] Chen-Hsuan Lin, Wei-Chiu Ma, Antonio Torralba, and Simon Lucey. BARF: Bundle-adjusting neural radiance fields. In *Proceedings of the IEEE/CVF International Conference on Computer Vision*, pages 5741–5751, 2021. 2
- [20] Chen-Hsuan Lin, Jun Gao, Luming Tang, Towaki Takikawa, Xiaohui Zeng, Xun Huang, Karsten Kreis, Sanja Fidler, Ming-Yu Liu, and Tsung-Yi Lin. Magic3D: High-resolution text-to-3d content creation. In *Proceedings of the IEEE/CVF Conference on Computer Vision and Pattern Recognition*, pages 300–309, 2023. 2
- [21] Xiaoxiao Long, Cheng Lin, Peng Wang, Taku Komura, and Wenping Wang. SparseNeuS: Fast generalizable neural surface reconstruction from sparse views. In *European Conference on Computer Vision*, pages 210–227. Springer, 2022. 2
- [22] Ben Mildenhall, Pratul P Srinivasan, Matthew Tancik, Jonathan T Barron, Ravi Ramamoorthi, and Ren Ng. NeRF: Representing scenes as neural radiance fields for view synthesis. *Communications of the ACM*, 65(1):99–106, 2021. 2, 3, 4, 7, 5
- [23] Ben Mildenhall, Dor Verbin, Pratul P. Srinivasan, Peter Hedman, Ricardo Martin-Brualla, and Jonathan T. Barron. MultiNeRF: A Code Release for Mip-NeRF 360, Ref-NeRF, and RawNeRF, 2022. 5
- [24] Thomas Müller, Alex Evans, Christoph Schied, and Alexander Keller. Instant neural graphics primitives with a multiresolution hash encoding. *SIGGRAPH*, 2022. 2, 3, 5, 7, 1

- [25] Jacob Munkberg, Jon Hasselgren, Tianchang Shen, Jun Gao, Wenzheng Chen, Alex Evans, Thomas Müller, and Sanja Fidler. Extracting triangular 3D models, materials, and lighting from images. In *Proceedings of the IEEE/CVF Conference on Computer Vision and Pattern Recognition*, pages 8280–8290, 2022. [6](#), [4](#)
- [26] Michael Niemeyer, Jonathan T Barron, Ben Mildenhall, Mehdi SM Sajjadi, Andreas Geiger, and Noha Radwan. Reg-NeRF: Regularizing neural radiance fields for view synthesis from sparse inputs. In *Proceedings of the IEEE/CVF Conference on Computer Vision and Pattern Recognition*, pages 5480–5490, 2022. [2](#)
- [27] Michael Oechsle, Songyou Peng, and Andreas Geiger. UNISURF: Unifying neural implicit surfaces and radiance fields for multi-view reconstruction. In *Proceedings of the IEEE/CVF International Conference on Computer Vision*, pages 5589–5599, 2021. [2](#)
- [28] Ben Poole, Ajay Jain, Jonathan T Barron, and Ben Mildenhall. DreamFusion: Text-to-3d using 2d diffusion. *arXiv preprint arXiv:2209.14988*, 2022. [2](#)
- [29] Christian Reiser, Rick Szeliski, Dor Verbin, Pratul Srinivasan, Ben Mildenhall, Andreas Geiger, Jon Barron, and Peter Hedman. MERF: Memory-efficient radiance fields for real-time view synthesis in unbounded scenes. *ACM Transactions on Graphics (TOG)*, 42(4):1–12, 2023. [2](#), [7](#)
- [30] Yufan Ren, Fangjinhua Wang, Tong Zhang, Marc Pollefeys, and Sabine Süsstrunk. Volrecon: Volume rendering of signed ray distance functions for generalizable multi-view reconstruction. *arXiv preprint arXiv:2212.08067*, 2022. [2](#)
- [31] Gernot Riegler and Vladlen Koltun. Stable view synthesis. In *Proceedings of the IEEE Conference on Computer Vision and Pattern Recognition*, 2021. [2](#)
- [32] Radu Alexandru Rosu and Sven Behnke. PermutoSDF: Fast multi-view reconstruction with implicit surfaces using permutohedral lattices. In *Proceedings of the IEEE/CVF Conference on Computer Vision and Pattern Recognition*, pages 8466–8475, 2023. [2](#), [5](#), [6](#), [3](#)
- [33] Johannes L Schönberger, Enliang Zheng, Jan-Michael Frahm, and Marc Pollefeys. Pixelwise view selection for unstructured multi-view stereo. In *Computer Vision–ECCV 2016: 14th European Conference, Amsterdam, The Netherlands, October 11–14, 2016, Proceedings, Part III 14*, pages 501–518. Springer, 2016. [2](#)
- [34] Edgar Sucar, Shikun Liu, Joseph Ortiz, and Andrew J Davison. iMAP: Implicit mapping and positioning in real-time. In *Proceedings of the IEEE/CVF International Conference on Computer Vision*, pages 6229–6238, 2021. [2](#)
- [35] Cheng Sun, Min Sun, and Hwann-Tzong Chen. Direct voxel grid optimization: Super-fast convergence for radiance fields reconstruction. In *Proceedings of the IEEE/CVF Conference on Computer Vision and Pattern Recognition*, pages 5459–5469, 2022. [2](#)
- [36] Prune Truong, Marie-Julie Rakotosaona, Fabian Manhardt, and Federico Tombari. SPARF: Neural radiance fields from sparse and noisy poses. In *Proceedings of the IEEE/CVF Conference on Computer Vision and Pattern Recognition*, pages 4190–4200, 2023. [2](#)
- [37] Dor Verbin, Peter Hedman, Ben Mildenhall, Todd Zickler, Jonathan T Barron, and Pratul P Srinivasan. Ref-NeRF: Structured view-dependent appearance for neural radiance fields. In *2022 IEEE/CVF Conference on Computer Vision and Pattern Recognition (CVPR)*, pages 5481–5490. IEEE, 2022. [1](#), [2](#), [3](#), [4](#), [5](#), [6](#), [7](#), [8](#)
- [38] Fangjinhua Wang, Silvano Galliani, Christoph Vogel, Pablo Speciale, and Marc Pollefeys. PatchmatchNet: Learned multi-view patchmatch stereo. In *Proceedings of the IEEE/CVF conference on computer vision and pattern recognition*, pages 14194–14203, 2021. [2](#)
- [39] Fangjinhua Wang, Silvano Galliani, Christoph Vogel, and Marc Pollefeys. IterMVS: Iterative probability estimation for efficient multi-view stereo. In *Proceedings of the IEEE/CVF conference on computer vision and pattern recognition*, pages 8606–8615, 2022. [2](#)
- [40] Peng Wang, Lingjie Liu, Yuan Liu, Christian Theobalt, Taku Komura, and Wenping Wang. NeuS: Learning neural implicit surfaces by volume rendering for multi-view reconstruction. *arXiv preprint arXiv:2106.10689*, 2021. [2](#), [4](#), [5](#), [6](#), [3](#)
- [41] Qingshan Xu and Wenbing Tao. Multi-scale geometric consistency guided multi-view stereo. *Computer Vision and Pattern Recognition (CVPR)*, 2019. [2](#)
- [42] Yao Yao, Zixin Luo, Shiwei Li, Tian Fang, and Long Quan. MVSNet: Depth inference for unstructured multi-view stereo. In *Proceedings of the European conference on computer vision (ECCV)*, pages 767–783, 2018. [2](#)
- [43] Lior Yariv, Jiatao Gu, Yoni Kasten, and Yaron Lipman. Volume rendering of neural implicit surfaces. *Advances in Neural Information Processing Systems*, 34:4805–4815, 2021. [2](#), [4](#), [5](#), [6](#), [3](#)
- [44] Lior Yariv, Peter Hedman, Christian Reiser, Dor Verbin, Pratul P Srinivasan, Richard Szeliski, Jonathan T Barron, and Ben Mildenhall. BakedSDF: Meshing neural sdfs for real-time view synthesis. *arXiv preprint arXiv:2302.14859*, 2023. [2](#), [4](#), [5](#), [6](#), [7](#), [1](#), [3](#)
- [45] Alex Yu, Ruilong Li, Matthew Tancik, Hao Li, Ren Ng, and Angjoo Kanazawa. PlenOctrees for real-time rendering of neural radiance fields. In *Proceedings of the IEEE/CVF International Conference on Computer Vision*, pages 5752–5761, 2021. [2](#)
- [46] Alex Yu, Vickie Ye, Matthew Tancik, and Angjoo Kanazawa. pixelNeRF: Neural radiance fields from one or few images. In *Proceedings of the IEEE/CVF Conference on Computer Vision and Pattern Recognition*, pages 4578–4587, 2021. [2](#)
- [47] Zehao Yu, Songyou Peng, Michael Niemeyer, Torsten Sattler, and Andreas Geiger. MonoSDF: Exploring monocular geometric cues for neural implicit surface reconstruction. *Advances in neural information processing systems*, 35:25018–25032, 2022. [2](#)
- [48] Kai Zhang, Gernot Riegler, Noah Snavely, and Vladlen Koltun. NeRF++: Analyzing and improving neural radiance fields. *arXiv preprint arXiv:2010.07492*, 2020. [7](#), [5](#)
- [49] Zihan Zhu, Songyou Peng, Viktor Larsson, Weiwei Xu, Hujun Bao, Zhaopeng Cui, Martin R Oswald, and Marc Pollefeys. NICE-SLAM: Neural implicit scalable encoding for

SLAM. In *Proceedings of the IEEE/CVF Conference on Computer Vision and Pattern Recognition*, pages 12786–12796, 2022. [2](#)

UniSDF: Unifying Neural Representations for High-Fidelity 3D Reconstruction of Complex Scenes with Reflections

Supplementary Material

In the supplementary document, we first discuss more implementation details of our method, including network architecture and training settings. Second, we discuss the baseline BakedSDF [44] in more detail. We show that BakedSDF is often not stable and we discuss how we fine-tune the method to improve performance on several scenes. Third, we summarize the detailed evaluation results for individual scenes on DTU [1], Shiny Blender [37], Mip-NeRF 360 [3] and Ref-NeRF real [37] datasets. We also qualitatively compare with the *finetuned* BakedSDF. Finally, we discuss the comparison with two custom baselines, RefV and CamV, in more details.

6. Implementation Details

6.1. Network Architecture

In addition to the iNGP [24] structure that we have introduced in the main paper, we further discuss the details of the MLP architectures. Specifically, the SDF MLP f has 2 layers with 256 hidden units and outputs the bottleneck feature vector \mathbf{b} with size 256. The two radiance MLP f_{cam} , f_{ref} have 4 layers with 256 hidden units. Besides, the weight MLP f_w has a single layer with 256 hidden units.

Recall that following Mip-NeRF 360 [3], we use two rounds of proposal sampling and then a final NeRF sampling round. The proposal sampling is used to bound the scene geometry and recursively generate more detailed sample intervals, while the final NeRF sampling is used to render the final set of intervals into an image. We set the number of samples for these 3 sampling rounds as 64, 32, 32 for the object-level DTU [1] and Shiny Blender [37], and 64, 64, 32 for unbounded Mip-NeRF 360 [3] and Ref-NeRF real [37] datasets.

In the Sec. 3 of the main paper, we mainly introduce model details of the final NeRF sampling round, where the color is rendered, for simplicity. Thus, we introduce the details for proposal sampling rounds here. Specifically, the proposal sampling rounds only have a SDF MLP, *i.e.* no radiance MLP and weight MLP, since color is not rendered in these rounds. Moreover, the two proposal sampling rounds share a SDF MLP, which is different from the SDF MLP in the NeRF sampling round. Contrary to Zip-NeRF [4] that uses a distinct iNGP for each sampling round, we use a single iNGP that is shared by all sampling rounds. We find that this produces similar performance as using multiple iNGPs but explicitly simplifies the model.

6.2. Training

In the loss function (Eq. 12 in the main paper, which is for the final NeRF sampling round), we set $\lambda_1 = 10^{-4}$ and $\lambda_3 = 10^{-3}$. Moreover, we set $\lambda_2 = 10^{-4}$ for Shiny Blender [37], and $\lambda_2 = 10^{-3}$ for DTU [1], Mip-NeRF 360 [3] and Ref-NeRF real [37] datasets. For proposal sampling rounds, we replace \mathcal{L}_{color} with \mathcal{L}_{prop} , the proposal loss described in Mip-NeRF 360 [3].

For training, we use the Adam [16] optimizer with $\beta_1 = 0.9$, $\beta_2 = 0.999$, $\epsilon = 10^{-6}$. We warm up the learning rate in the first 2% iterations and then decay the it logarithmically from 5×10^{-3} to 5×10^{-4} .

7. Baselines

As we discuss in the main paper, the optimization of BakedSDF [44] is sensitive and often fails completely on Shiny Blender [37] and Ref-NeRF real dataset [37], as shown in Fig. 12.

BakedSDF only uses eikonal loss, \mathcal{L}_{eik} , for regularization, where the corresponding loss weight is set to 0.1 by default. We experimentally find that decreasing the eikonal loss weight can stabilize the training and thus carefully tune it for each scene. For Shiny Blender [37], we set the eikonal loss weight as 10^{-2} for “toaster”, “helmet” and “coffee”, and 10^{-1} for “ball”. Unfortunately, we could not find the best eikonal loss weight for “car” and “teapot” scenes and the training keeps failing. For Ref-NeRF real dataset [37], we set the eikonal loss weight as 10^{-2} for “sedan” and “toy-car”, and 10^{-5} for “garden spheres”.

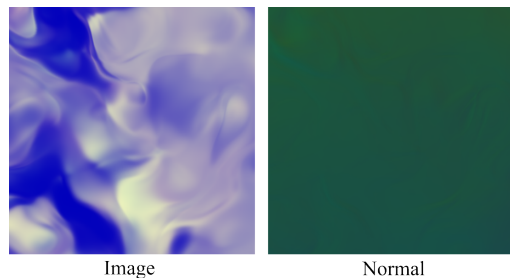


Figure 12. Final image rendering and normal of original BakedSDF [44] on “garden spheres” scene [37]. The training fails completely.

8. Detailed Evaluation Results

Tables 6, 7, 8 and 9 contain the detailed metrics for each individual scene on DTU [1], Shiny Blender [37], Mip-NeRF

360 [3] and Ref-NeRF real [37] datasets respectively.

On Ref-NeRF real dataset, we qualitatively compare with our *finetuned* BakedSDF on “garden spheres” in Fig. 13. The *finetuned* BakedSDF has small artifacts on the spheres and fails to reconstruct fine geometric details of the statue as well as the ground, while our method reconstructs the reflective spheres and the fine geometric details better. Additionally, we compare with different methods [17, 37, 44] on “toy-car” scene, as shown in Fig. 14. The *finetuned* BakedSDF successfully reconstructs the smooth surface, but contains artifacts on the plate as highlighted. Neuralangelo [17] reconstructs a large floater around the steering wheel.

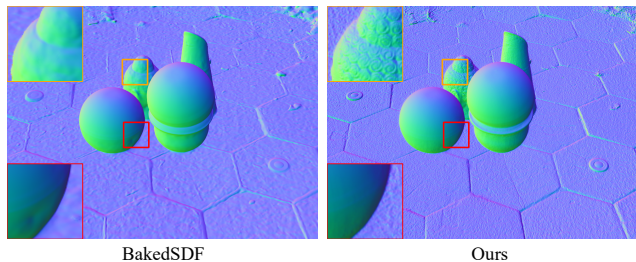


Figure 13. Qualitative comparison with the *finetuned* BakedSDF [44] on “garden spheres” scene [37]. BakedSDF has small artifacts on the spheres and oversmooths the geometry details of statue and ground. Best viewed when zoomed in.

9. Custom Baselines Comparison

In the main paper, we have compared our method with two custom baselines, CamV and RefV, both quantitatively (Table 5) and qualitatively (Fig. 8).

In Fig. 15, we further visualize the qualitative results on scan 37 of DTU [1]. On the one hand, RefV reconstructs holes on the objects with or without reflections, which is similar to the artifacts that BakedSDF [44] shows in Fig. 7 of the main paper. On the other hand, though the surface is a little noisy, CamV reconstructs shiny objects relatively well. Note that in Fig. 8 of the main paper, CamV also reconstructs the shiny surfaces of “toy-car” well, despite having some small artifacts. Since scan 37 of DTU and “toy-car” of Ref-NeRF real dataset mainly contain reflective surfaces that are less specular, we can infer that camera view radiance field can handle less specular reflections to some extent.

As shown in Fig. 16, we sometimes observe that RefV has optimization issues with separate diffuse and specular components. Specifically, the specular component may be empty throughout training, while the diffuse component represents both view-dependent and non view-dependent appearance. Since diffuse component depends only on the 3D position \mathbf{x} , the view-dependence is represented with incorrect geometry, as shown in the results of “toy-car” in

Fig. 16. We believe that this issue may be related to the high frequency signals that iNGP [24] can encode. In RefV, the diffuse component is parameterized by the feature vector γ from iNGP, which is capable of representing very high frequency signal. Therefore, the diffuse component may take advantage of the high capacity of the iNGP representation to model the view-dependent appearance with geometry only, leading to an incorrect reconstruction. This is especially true for small-scale scenes with relatively simple view-dependent appearance, e.g. “toy-car”.

Methods	24	37	40	55	63	65	69	83	97	105	106	110	114	118	122
VolSDF [43]	1.14	1.26	0.81	0.49	1.25	0.70	0.72	1.29	1.18	0.70	0.66	1.08	0.42	0.61	0.55
NeuS [40]	1.37	1.21	0.73	0.40	1.20	0.70	0.72	1.01	1.16	0.82	0.66	1.69	0.39	0.49	0.51
NeuralWarp [10]	0.49	0.71	0.38	0.38	0.79	0.81	0.82	1.20	1.06	0.68	0.66	0.74	0.41	0.63	0.51
Neuralangelo [17]	0.49	1.05	0.95	0.38	1.22	1.10	2.16	1.68	1.78	0.93	0.44	1.46	0.41	1.13	0.97
PermutoSDF [32]	0.52	0.75	0.41	0.37	0.90	0.66	0.59	1.37	1.07	0.85	0.46	0.98	0.33	0.39	0.50
Ours	0.54	0.84	0.66	0.51	0.76	0.64	0.71	0.70	0.86	0.57	0.69	0.65	0.45	0.56	0.50

Table 6. Quantitative Chamfer distance results of individual scenes on DTU dataset [1]. Red and orange indicate the first and second best performing algorithms for each scene.

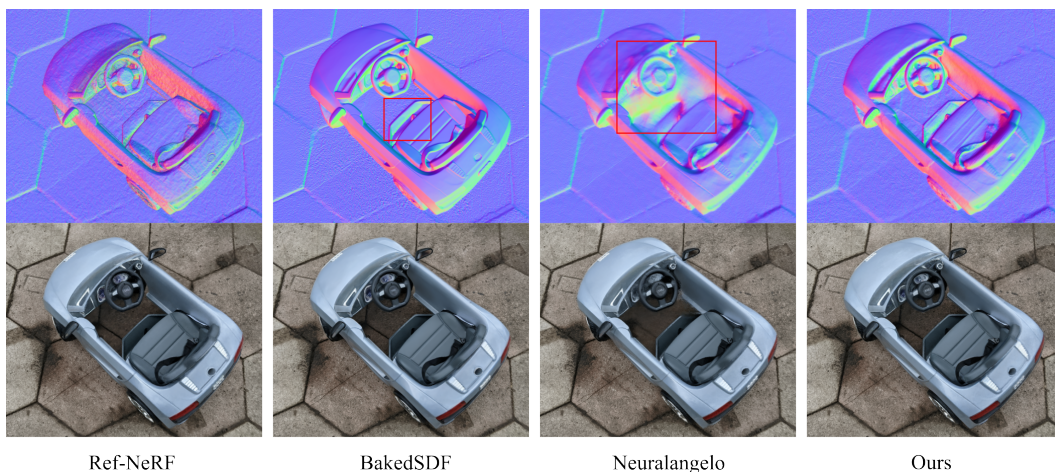


Figure 14. Qualitative comparison with Ref-NeRF [37], BakedSDF [44] and Neuralangelo [17] on “toycar” scene [37]. The *finetuned* BakedSDF has artifacts on the plate, while Neuralangelo has a large floater around the steering wheel (both are highlighted with red boxes). Best viewed when zoomed in.

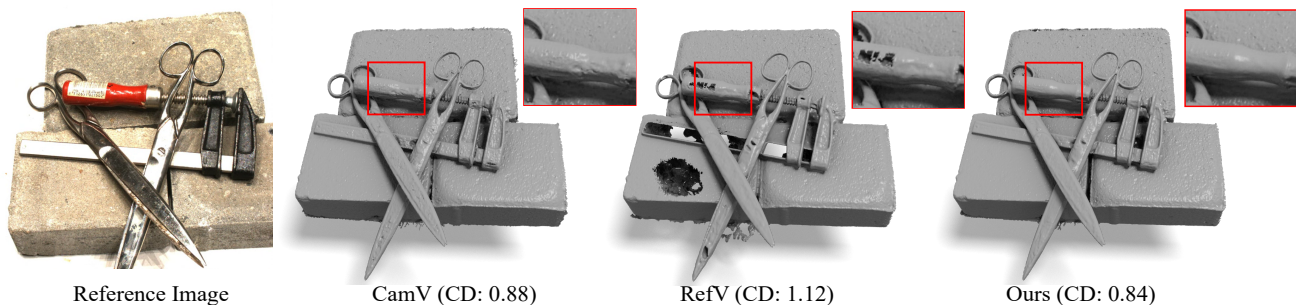


Figure 15. Comparison with two baselines, CamV and RefV, on scan 37 of DTU [1] (CD is Chamfer distance error). CamV reconstructs more noisy surface on the red handle with reflections (highlighted with red box and zoomed in), while RefV generates holes on the shiny objects and even the brick without any reflections. Best viewed when zoomed in.

Methods	car	ball	helmet	teapot	toaster	coffee
PSNR \uparrow						
NVDiffRec [25]	27.98	21.77	26.97	40.44	24.31	30.74
Ref-NeRF [37]	30.82	47.46	29.68	47.90	25.70	34.21
BakedSDF [44]	-	31.35	35.50	-	23.84	35.06
ENVIDR [18]	29.88	41.03	36.98	46.14	26.63	34.45
Ours	29.86	44.10	38.84	48.76	26.18	33.17
SSIM \uparrow						
NVDiffRec [25]	0.963	0.858	0.951	0.996	0.928	0.973
Ref-NeRF [37]	0.955	0.995	0.958	0.998	0.922	0.974
BakedSDF [44]	-	0.979	0.990	-	0.939	0.978
ENVIDR [18]	0.972	0.997	0.993	0.999	0.955	0.984
Ours	0.954	0.993	0.990	0.998	0.945	0.973
LPIPS \downarrow						
NVDiffRec [25]	0.045	0.297	0.118	0.011	0.169	0.076
Ref-NeRF [37]	0.041	0.059	0.075	0.004	0.095	0.078
BakedSDF [44]	-	0.094	0.019	-	0.079	0.072
ENVIDR [18]	0.031	0.020	0.022	0.003	0.097	0.044
Ours	0.047	0.039	0.021	0.004	0.072	0.078
MAE^o \downarrow						
NVDiffRec [25]	11.78	32.67	21.19	5.55	16.04	15.05
Ref-NeRF [37]	14.93	1.55	29.48	9.23	42.87	12.24
BakedSDF [44]	-	0.44	1.74	-	12.24	3.31
ENVIDR [18]	7.10	0.74	1.66	2.47	6.45	9.23
Ours	6.88	0.45	1.72	2.80	8.71	8.00

Table 7. Quantitative results of individual scenes on Shiny Blender [37]. Note that BakedSDF [44] fails on “car” and “teapot” scenes. Red, orange, and yellow indicate the first, second, and third best performing algorithms for each scene.

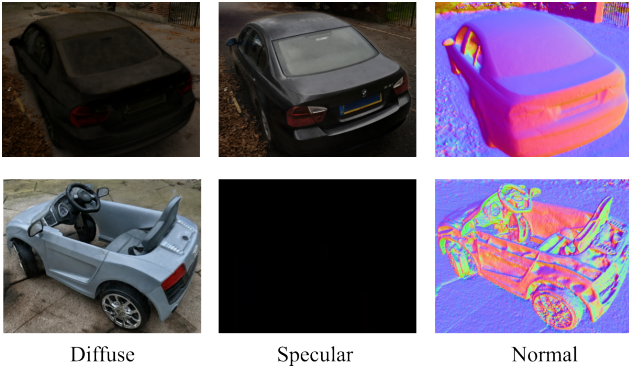


Figure 16. Visualization of diffuse color component, specular color component and normal for RefV on “sedan” and “toycar” scenes [37]. RefV successfully decomposes two color components for “sedan”, while it fails on “toycar” with blank specular component. Best viewed when zoomed in.

PSNR	Outdoor					Indoor			
	<i>bicycle</i>	<i>flowers</i>	<i>garden</i>	<i>stump</i>	<i>treehill</i>	<i>room</i>	<i>counter</i>	<i>kitchen</i>	<i>bonsai</i>
NeRF [22]	21.76	19.40	23.11	21.73	21.28	28.56	25.67	26.31	26.81
NeRF++ [48]	22.64	20.31	24.32	24.34	22.20	28.87	26.38	27.80	29.15
Mip-NeRF 360 [3]	24.40	21.64	26.94	26.36	22.81	31.40	29.44	32.02	33.11
Instant NGP [24]	22.79	19.19	25.26	24.80	22.46	30.31	26.21	29.00	31.08
Zip-NeRF [4]	25.80	22.40	28.20	27.55	23.89	32.65	29.38	32.50	34.46
BakedSDF [44]	23.05	20.55	26.44	24.39	22.55	30.68	27.99	30.91	31.26
Ours	24.67	21.83	27.46	26.39	23.51	31.25	29.26	31.73	32.86

SSIM	Outdoor					Indoor			
	<i>bicycle</i>	<i>flowers</i>	<i>garden</i>	<i>stump</i>	<i>treehill</i>	<i>room</i>	<i>counter</i>	<i>kitchen</i>	<i>bonsai</i>
NeRF [22]	0.455	0.376	0.546	0.453	0.459	0.843	0.775	0.749	0.792
NeRF++ [48]	0.526	0.453	0.635	0.594	0.530	0.852	0.802	0.816	0.876
Mip-NeRF 360 [3]	0.693	0.583	0.816	0.746	0.632	0.913	0.895	0.920	0.939
Instant NGP [24]	0.540	0.378	0.709	0.654	0.547	0.893	0.845	0.857	0.924
Zip-NeRF [4]	0.769	0.642	0.860	0.800	0.681	0.925	0.902	0.928	0.949
BakedSDF [44]	0.588	0.504	0.793	0.662	0.543	0.892	0.845	0.903	0.911
Ours	0.737	0.606	0.844	0.759	0.670	0.914	0.888	0.919	0.939

LPIPS	Outdoor					Indoor			
	<i>bicycle</i>	<i>flowers</i>	<i>garden</i>	<i>stump</i>	<i>treehill</i>	<i>room</i>	<i>counter</i>	<i>kitchen</i>	<i>bonsai</i>
NeRF [22]	0.536	0.529	0.415	0.551	0.546	0.353	0.394	0.335	0.398
NeRF++ [48]	0.455	0.466	0.331	0.416	0.466	0.335	0.351	0.260	0.291
Mip-NeRF 360 [3]	0.289	0.345	0.164	0.254	0.338	0.211	0.203	0.126	0.177
Instant NGP [24]	0.398	0.441	0.255	0.339	0.420	0.242	0.255	0.170	0.198
Zip-NeRF [4]	0.208	0.273	0.118	0.193	0.242	0.196	0.185	0.116	0.173
BakedSDF [44]	0.400	0.437	0.204	0.343	0.471	0.270	0.293	0.165	0.244
Ours	0.243	0.320	0.136	0.242	0.265	0.206	0.206	0.124	0.184

Table 8. Quantitative results of individual scenes on Mip-NeRF 360 dataset [3]. Red, orange, and yellow indicate the first, second, and third best performing algorithms for each scene.

Methods	Sedan			Toycar			Garden Spheres		
	PSNR \uparrow	SSIM \uparrow	LPIPS \downarrow	PSNR \uparrow	SSIM \uparrow	LPIPS \downarrow	PSNR \uparrow	SSIM \uparrow	LPIPS \downarrow
Mip-NeRF 360 [3]	25.56	0.708	0.304	24.32	0.654	0.256	22.94	0.587	0.268
Ref-NeRF [37]	25.20	0.639	0.406	24.40	0.627	0.292	22.57	0.502	0.366
Zip-NeRF [4]	25.85	0.733	0.260	23.41	0.626	0.243	21.77	0.545	0.238
Neuralangelo [17]	24.82	0.656	0.384	24.28	0.638	0.293	22.03	0.529	0.313
BakedSDF [44]	25.70	0.700	0.332	24.51	0.655	0.280	23.08	0.553	0.363
ENVDR [18]	-	-	-	-	-	-	22.67	0.550	0.312
Ours	24.68	0.700	0.309	24.15	0.639	0.245	22.27	0.567	0.243

Table 9. Quantitative results of individual scenes on the Ref-NeRF real dataset [37]. Since ENVDR [18] is unable to handle unbounded scenes, we report the results of “garden spheres” from their paper. Red, orange, and yellow indicate the first, second, and third best performing algorithms for each metric.